Available online at www.sciencedirect.com
ScienceDirect
Trans. Nonferrous Met. Soc. China 32(2022) 1501−1512
Transactions of Nonferrous Metals Society of China
www.tnmsc.cn

Effect of Nd addition on microstructure and tensile properties of laser additive manufactured TC11 titanium alloy

Wen-gao YAN[1], Hua-ming WANG[1], Hai-bo TANG[1,2], Xu CHENG[1,2], Yan-yan ZHU[1,2]

1. National Engineering Laboratory of Additive Manufacturing for Large Metallic Components, Research Institute for Frontier Science, Beihang University, Beijing 100191, China;
2. Ningbo Institute of Technology, Beihang University, Ningbo 315800, China

Received 9 March 2021; accepted 17 March 2022

Abstract: Single-layer and multilayer laser additive manufacturing (LAM) for TC11 alloy with different Nd additions was conducted and the effect of Nd addition on microstructure and properties was studied. With the addition of Nd, the aspect ratio of melting pools of single-layer specimens increases and the columnar-to-equiaxed transition occurs. The original β grain size and α plate width of TC11−1.0Nd are significantly reduced compared with those of pure TC11 specimens. It is proposed that the evenly distributed fine Nd_2O_3 precipitates of about 1.51 μm are formed preferentially during rapid solidification of melting pool, and they serve as heterogeneous nucleation particles to refine the microstructure in the subsequent solidification and solid-state phase transformation. Due to the multiple effects of Nd on the microstructure, the ultimate tensile strength of TC11−1.0Nd increases, while the yield strength, ductility and microhardness decrease compared with those of pure TC11.

Key words: laser additive manufacturing; titanium alloy; rare-earth element; microstructure; grain refinement; mechanical properties

1 Introduction

Titanium and titanium alloys are widely used in industrial applications because of their extraordinary properties, such as high specific strength and good corrosion resistance [1,2]. Nowadays, aerospace development puts forward higher requirements for advanced equipment with outstanding performance. Therefore, there is a strong demand for titanium alloys with high-temperature resistance, high strength, and increased damage tolerance.

Trace addition of rare-earth elements in titanium alloys is one of the most effective methods to improve their mechanical properties substantially. Rare-earth elements can combine with oxygen or other alloying elements to form second-phase particles which are very stable at elevated temperatures [3,4]. Some authors have proven that these high-temperature stable second-phase particles can refine the prior β-Ti grains, resulting in simultaneous improvement of ambient temperature strength and ductility of alloys [4−6]. These particles can hinder the movement of dislocation, thereby improving the elevated temperature strength and creep resistance of alloys [7−9]. However, it is challenging to produce rare-earth second-phase particles of desired size and distribution by conventional casting technique because slow cooling rate can result in coarsening and segregation of the second-phase particles [10].

Rapid solidification provides an effective way to solve this problem. At an extremely fast cooling rate, high solid solubility of rare-earth elements in titanium alloys is acquired. This nonequilibrium

Corresponding author: Yan-yan ZHU, Tel: +86-13811024443, E-mail: zhuyy@buaa.edu.cn
DOI: 10.1016/S1003-6326(22)65889-8

supersaturated solid solution will decompose to form fine and uniform second-phase particles at a certain temperature [10−12]. SASTRY et al [10] have produced fine (<50 nm) rare-earth second-phase particles in Ti−RE (RE=Ce, Dy, Er, Gd, La, Nd, and Y) alloys by rapid solidification processing. But these rapid solidification processing methods, such as electron beam melting and splat quenching, can only produce alloy flakes or bands directly, which are not efficient for producing components [9,11]. So, a more efficient rapid solidification processing method is needed to produce rare-earth element added titanium alloys.

Laser additive manufacturing (LAM) is an advanced technology that can achieve the fully dense formation of near-net-shape metallic components directly based on layer-upon-layer deposition [13]. During LAM processing, each area under laser irradiation can form a tiny melting pool in which the molten metal undergoes an extraordinary, nonequilibrium, and rapid solidification processing [14,15]. Therefore, LAM has the characteristics of rapid solidification. Many researchers have successfully used this method to add trace elements to titanium alloys such as B, Zr, and Si [16−18]. In addition, LAM can efficiently achieve material preparation and component forming at the same time [17,19]. So, LAM can provide an efficient method for producing the rare-earth element added titanium alloys with unique merits.

Ti−6.5Al−3.5Mo−1.5Zr−0.3Si (named TC11 in China) is a typical α+β titanium alloy with a medium alloying extent [20]. The preparation of LAM TC11 is relatively mature. The mechanical properties of LAM TC11 are comparable to those of forging TC11 and even exceed forgings in terms of fracture toughness [20−22]. Thereby, the LAM TC11 is the ideal matrix for this study. In the present study, TC11 alloys containing different extents of neodymium (Nd) were synthesized by LAM processing to investigate the effects of Nd addition on the microstructure and mechanical properties of LAM TC11 alloy.

2 Experimental

2.1 Laser additive manufacturing

TC11 powders (99 wt.%, 74−300 μm) and Nd powders (99 wt.%, 74−300 μm) were mechanically mixed into powder of TC11−xNd (x=0.0, 0.1, 0.2, 0.4, 0.8, 1.0, 2.0, wt.%) as raw materials, with their morphologies shown in Fig. 1. During LAM processing, each layer would experience multiple thermal cycles, which made microstructure evolution very complicated. To investigate the microstructure evolution in each layer during solidification more directly, a set of single-track and single-layer LAM experiments were firstly conducted with mixed raw material powder laid in grooves of the substrate in advance (as shown in Fig. 2(a)). After that, to further study the effect of Nd addition on the microstructure and properties of the alloys after several thermal cycles, the compositions of TC11−1.0Nd and pure TC11 were selected to manufacture thick plate-like specimens with the geometric size of 80 mm × 20 mm × 8 mm

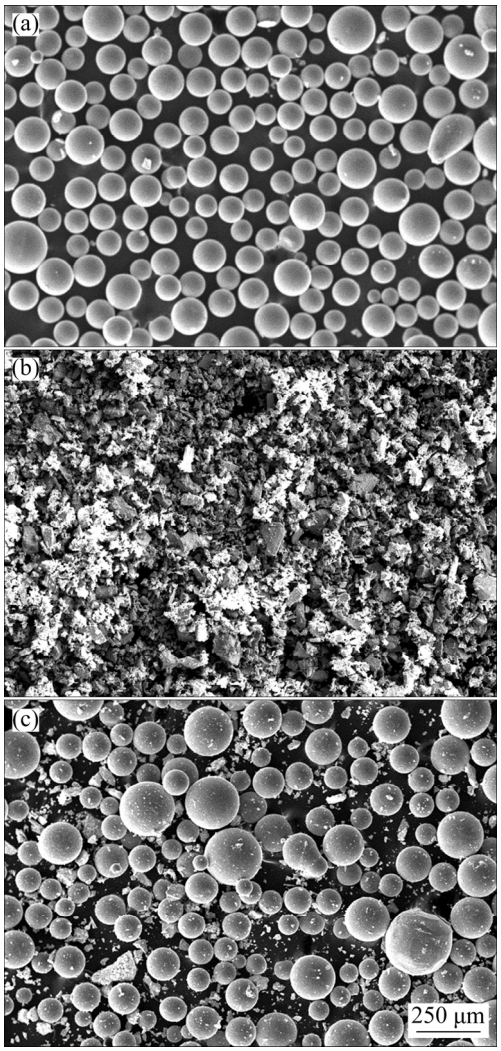

Fig. 1 Secondary electron SEM images of pure TC11 powder (a), pure Nd powder (b), and mixed powder (TC11−1.0Nd) (c)

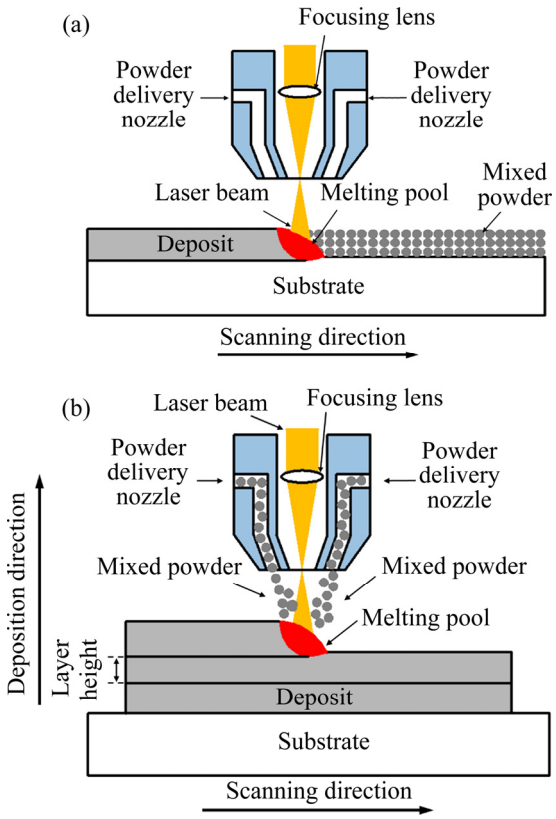

Fig. 2 Schematic diagrams of single-track and single-layer LAM experiment (a) and single-track and multi-layer LAM experiment (b)

by single-track and multilayer LAM experiments (as shown in Fig. 2(b)). In multilayer experiments, coaxial powder feeding technology was used with a powder delivery rate of 500−1000 g/h. The remaining parameters were the same for both kinds of experiments, as follows: laser beam power of 6 kW, scanning speed of 1000 mm/min, and beam diameter of 8 mm. To prevent the entry of foreign gas impurity, the whole experiment procedures were under an argon atmosphere (w(oxygen)< 50×10^{-5}).

2.2 Material characterization and tensile testing

Metallographic specimens of LAM TC11−xNd were prepared by standard methods. The specimens were sanded with sandpaper and polished with flannelette. Kroll's reagent (5 vol.% HF, 10 vol.% HNO_3 and 85 vol.% H_2O) was used to etch the specimens for 5−10 s. Then, the microstructure of specimens was characterized by optical microscopy (OM, LEICA−DM4000), scanning electron microscopy (ZEISS−Gemini 300) equipped with energy-dispersive spectroscopy. The phases were identified by X-ray diffraction (XRD), which was conducted on Rigaku D/max−2200pc automatic diffractometer with monochromatic Cu K_α radiation.

The microhardness of multilayer specimens was characterized by a HAZ−1000 semiautomatic Vickers tester with a dwell time of 10 s and a test load of 500 g. The tensile testing of multilayer specimens was carried out according to the test standard ISO 6892: 1998. The principal direction of tensile specimens was vertical to the deposition direction of multilayer specimens, and three tensile specimens were tested for an average. These tensile specimens were cylindrical with an overall length of 47 mm.

3 Results

3.1 Microstructure evolution

The morphologies of transverse cross sections (perpendicular to the scanning direction) of single-layer experiments are shown in Fig. 3. There are no equiaxed grains in pure TC11 specimens while increasing amounts of equiaxed grains appear at the top of melting pools with the addition of Nd. Some geometrical parameters of these melting pools were measured, including depth of equiaxed grains zone (D_e) and depth of columnar grains zone (D_c). The overall depth (D) is equal to the sum of D_e and D_c. In the pure TC11 specimen, D is equal to D_c as there are no equiaxed grains. The change tendency of D_e, D_c and D with the addition of Nd is shown in Fig. 4(a). When the addition of Nd is lower than 0.4 wt.%, three kinds of geometrical parameters show an overall upward trend with the addition of Nd. After that, with the addition of Nd continuing to increase, these geometrical parameters change little. Since the equiaxed grains on the top of the melting pool hinder the growth of columnar grains in TC11−0.1Nd, the D_c of TC11−0.1Nd is less than that in pure TC11. By calculating the depth ratio of the equiaxed grains zone (D_e/D), it is found that the fraction of equiaxed grains in melting pools is gradually increased with the addition of Nd (Fig. 4(b)). It is also noted that some cracks exist at the grain boundaries, resulting from the internal stress caused by the rapid cooling rate during the single-layer experiment.

Figure 5 shows the backscattered electron images for the microstructure of single-layer specimens. In Fig. 5, the bright white dots are the

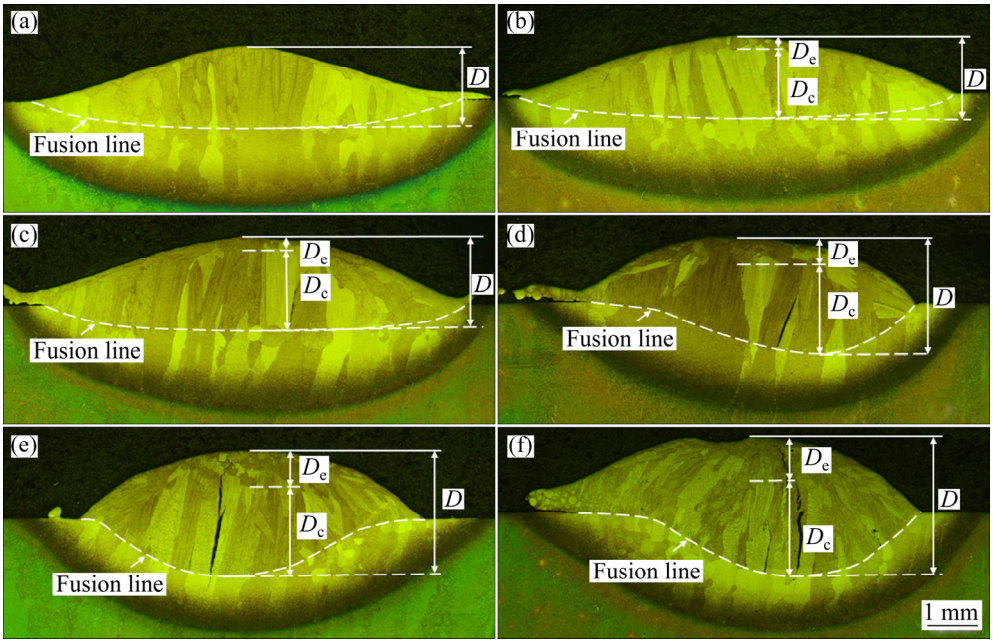

Fig. 3 OM micrographs showing shape of melting pool and cracks on transverse cross-sections of single-layer experiments with different additions of Nd: (a) Pure TC11; (b) TC11−0.1Nd; (c) TC11−0.2Nd; (d) TC11−0.4Nd; (e) TC11−1.0Nd; (f) TC11−2.0Nd

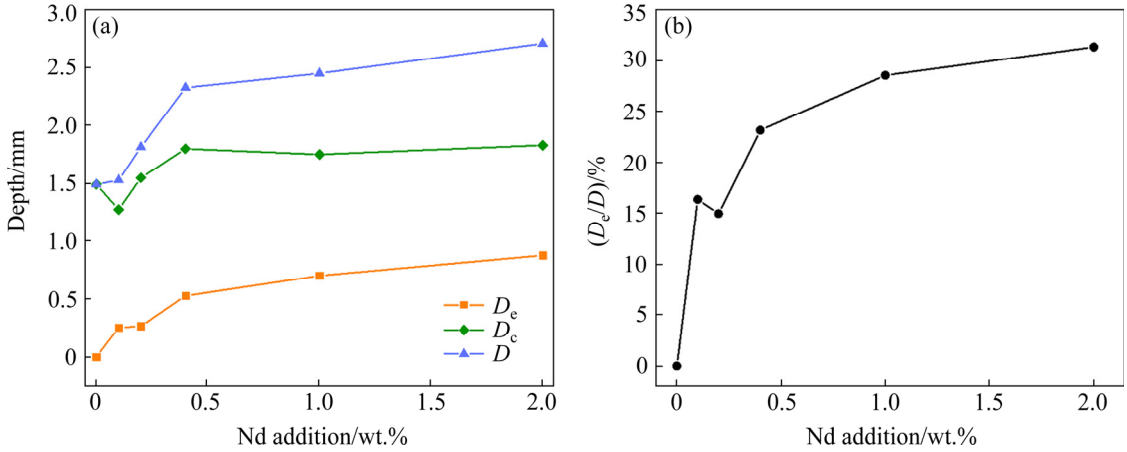

Fig. 4 Some geometrical parameters of melting pools as function of Nd addition: (a) D_e, D_c and D; (b) D_e/D

Nd-contained precipitates, while the black dots are the pits left by Nd-contained precipitates falling off during sanding or polishing. With the addition of Nd, more and more Nd-contained precipitates appear in these Nd added alloys, and many precipitates are distributed at the sub-boundary along the growth direction of the β-Ti grain, which makes the sub-boundary observable. When the addition of Nd reaches 1.0 wt.%, the dendrite arms are clearly visible (Fig. 5(d)).

The macrostructures of the transverse cross-sections (perpendicular to the scanning direction) of the multilayer specimens are shown in Fig. 6. It can be observed that the specimens consist of columnar grains, and no cracks exist in the specimens. Compared to the columnar grains in pure TC11 specimen, the columnar grains in TC11−1.0Nd specimen are refined. The microstructures of the transverse cross-sections of the multilayer specimens are also shown in Fig. 6. It is worth noting that the β grains in TC11−1.0Nd are refined, and the width of α plates in TC11−1.0Nd is less than that in pure TC11 specimen (Fig. 6). The average diameters of β grains and the average widths of α plates for these two specimens are listed in Table 1.

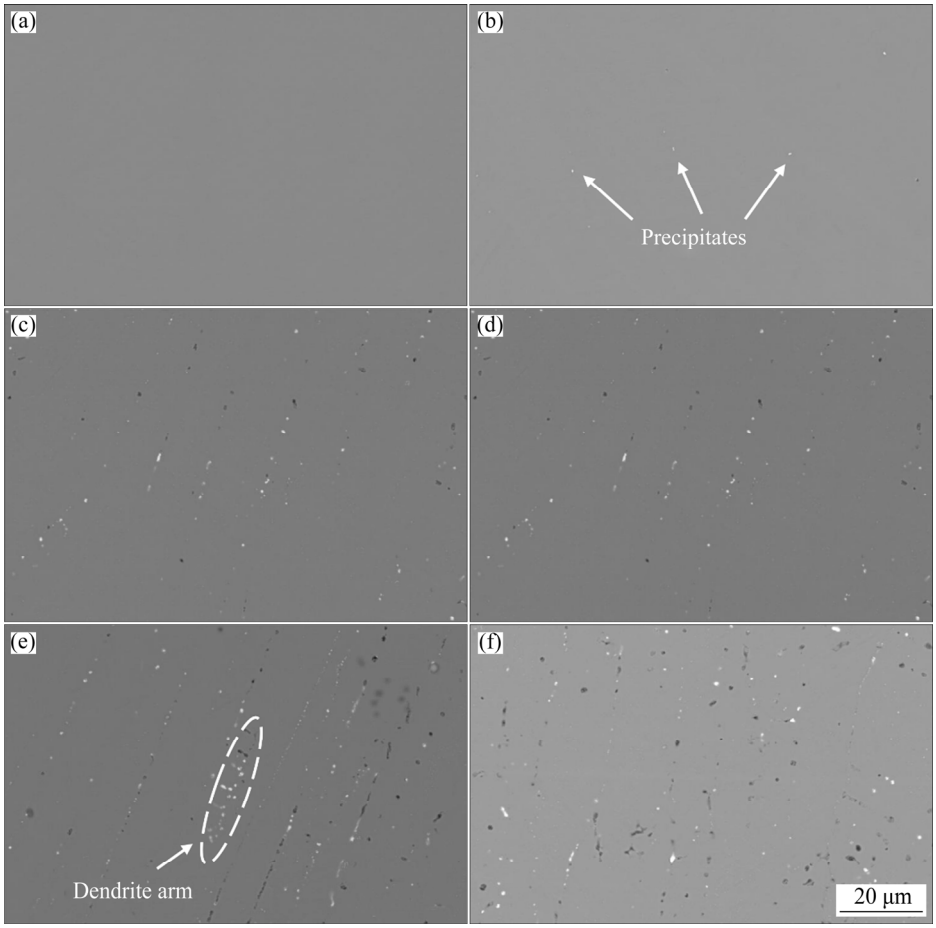

Fig. 5 Backscattered electron images showing microstructure of single-layer specimens: (a) Pure TC11; (b) TC11−0.1Nd; (c) TC11−0.2Nd; (d) TC11−0.4Nd; (e) TC11−1.0Nd; (f) TC11−2.0Nd

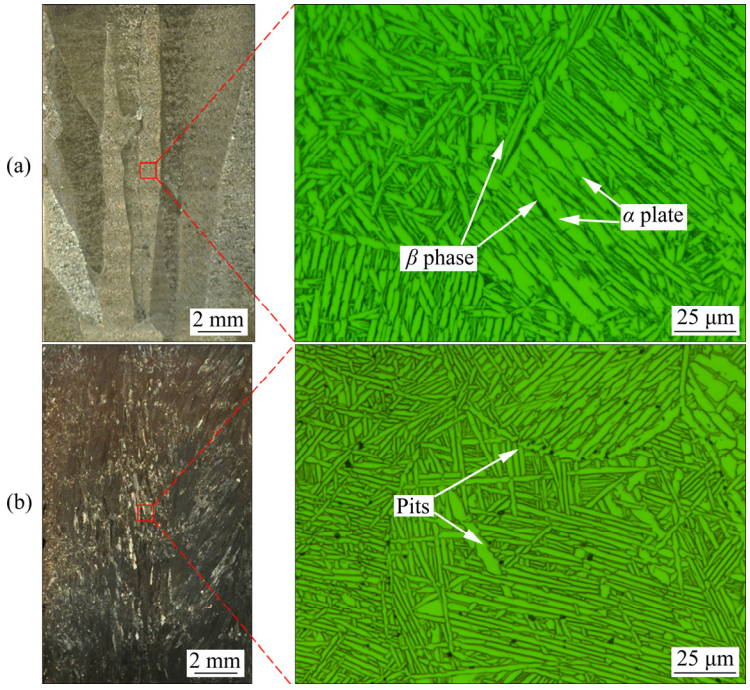

Fig. 6 OM micrographs showing macrostructure and microstructure of transverse cross-sections of multilayer specimens: (a) Pure TC11; (b) TC11−1.0Nd

Table 1 Average diameter of β grains and average width of α plates of pure TC11 and TC11−1.0Nd multilayer specimens

Alloy	Diameter of β grains/μm	Width of α plates/μm
Pure TC11	518±249	0.91±0.20
TC11−1.0Nd	150±71	0.46±0.23

The backscattered electron images in Fig. 7(a) show the morphology of Nd-contained precipitates in the TC11−1.0Nd multilayer specimen. The Nd-contained precipitates are evenly distributed without segregation. Most of these precipitates are spherical. The mean planar interparticle spacing and the mean diameter of particles for these precipitates are 1.51 and 0.1 μm, respectively.

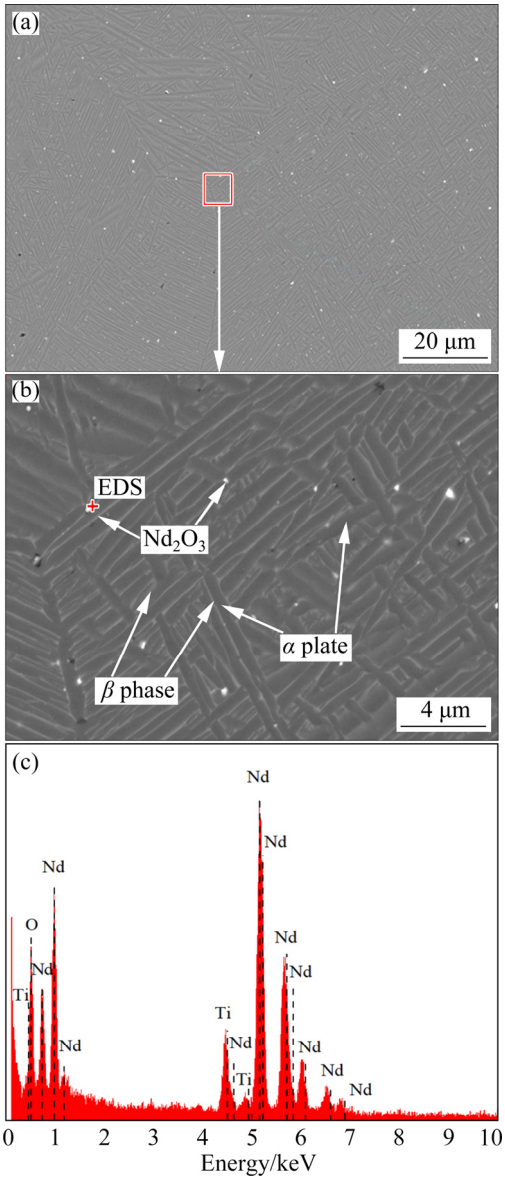

Fig. 7 Backscattered electron images showing microstructure of TC11−1.0Nd multilayer specimen (a, b) and EDS results of Na-contained precipitates (c)

ZHU et al [23] and LI et al [24] have proven that Nd has a strong affinity with oxygen so that it is inclined to combine with oxygen to form Nd_2O_3 oxides in titanium. So, the Nd-contained precipitates in TC11−1.0Nd multilayer specimen may be Nd_2O_3 particles. To prove this, X-ray diffraction (XRD) was used to identify the phases of the multilayer specimens, and the result is shown in Fig. 8. As seen in Fig. 8, the Nd_2O_3 peaks appear on the XRD pattern of TC11−1.0Nd, which proves that Nd_2O_3 oxides are formed in Nd-added TC11 alloy. In addition, compared to the XRD pattern of pure TC11, the peaks of the α-Ti and the β-Ti phases of TC11−1.0Nd shift slightly to the right, which indicates that the lattice constant of α phase and β phase in TC11−1.0Nd multilayer specimen decreases. Figure 7(c) shows the spot EDS of an Nd-contained precipitate in the TC11−1.0Nd multilayer specimen, which proves that most of the elements in the precipitate are Nd and O. So, the Nd-contained precipitates in TC11−1.0Nd multi- layer specimen are Nd_2O_3.

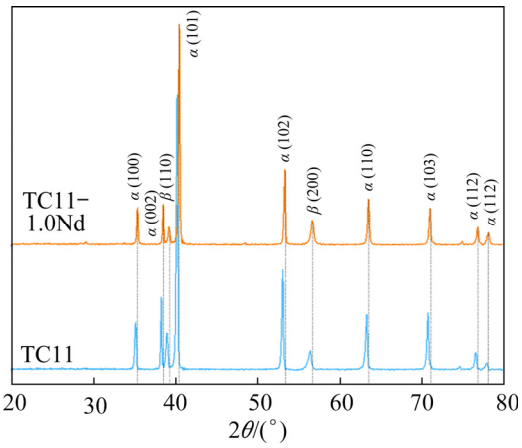

Fig. 8 XRD patterns of pure TC11 and TC11−1.0Nd multilayer samples

3.2 Mechanical properties

Table 2 gives the mechanical properties of multilayer specimens, including ultimate tensile strength (UTS), yield strength (YS), relative elongation (δ), fracture surface shrinkage (ψ), and microhardness of matrix. The stress−strain curves of three tensile specimens of TC11−1.0Nd and three tensile specimens of pure TC11 are shown in Fig. 9. Compared with pure TC11, the tensile strength of TC11−1.0Nd increases while the yield strength,

Table 2 Mechanical properties of multilayer specimens

Alloy	UTS/MPa	YS/MPa	δ/%
Pure TC11	991±15	921±19	13.8±1.3
TC11−1.0Nd	1037±54	909±3	7.7±1
Alloy	ψ/%	Microhardness (HV)	
Pure TC11	48.7±6.1	364±6	
TC11−1.0Nd	18.0±1.5	336±10	

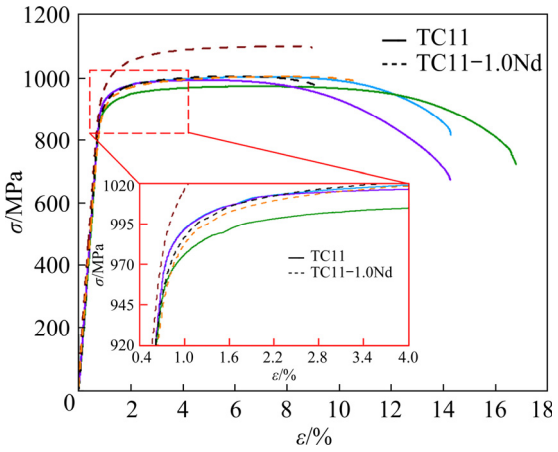

Fig. 9 Stress−strain curves of three tensile specimens of TC11−1.0Nd and three tensile specimens of pure TC11

ductility, and hardness decrease. Figure 10 shows the fractograph of these tensile specimens. The macroscopic fracture morphology of pure TC11 is a typical ductile cup cone fracture with obvious necking and shear lips. As for TC11−1.0Nd, the fracture surface also has shear lips, but the necking is not as obvious as pure TC11. The microscopic fractures of pure TC11 and TC11−1.0Nd are characterized by dimpled rupture. But the dimples of pure TC11 are deeper than those of TC11−1.0Nd. Besides, the dimples of TC11−1.0Nd have some broken Nd_2O_3 particles located in the center of dimples.

4 Discussion

As shown in Figs. 3 and 4, the added Nd makes the melting pool deeper. According to the Heiple−Roper theory, the thermocapillary force dominates the fluid flow in melting pool and thus the shape of melting pool [25−27]. In laser welding, the Marangoni effect determined by surface tension is the most critical factor for the morphology of the melting pool. The surface tension gradient exists on the melting pool surface because the surface tension of molten metal is temperature-dependent. In general, the surface tension of pure liquid metal is negatively related to the temperature. So, the surface tension of the pure metal melting pool decreases from edge to center. The convection of the melting pool is shown in Fig. 11(a). But when the melting pool contains some surface-active element (such as O, S and Te), which can alter the temperature coefficient of surface tension or even alter it from negative to positive [26,27], the

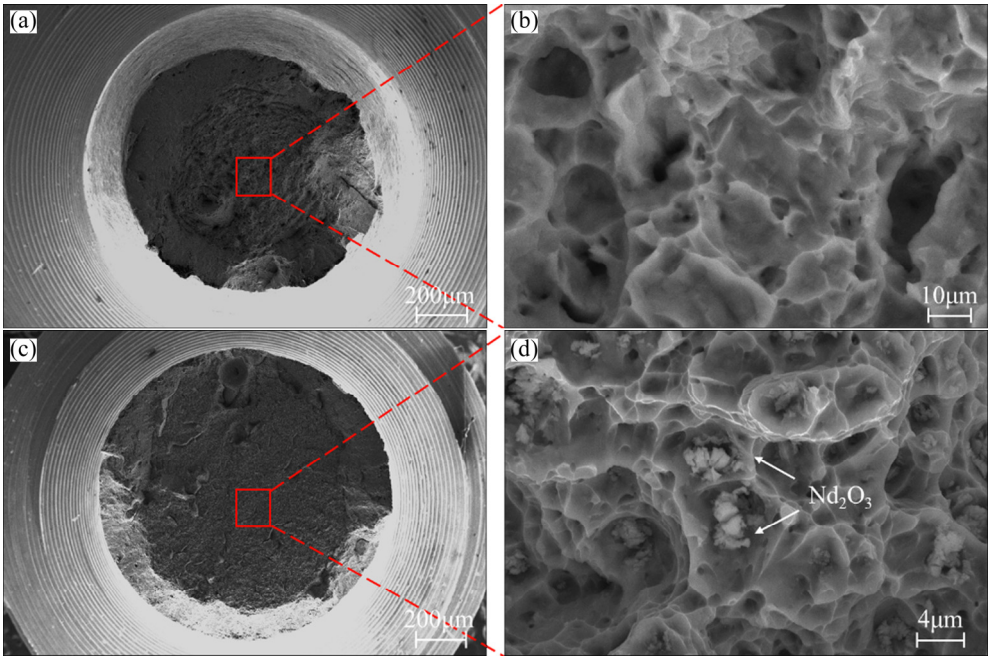

Fig. 10 Secondary electron images showing fractograph of multilayer specimens: (a, b) Pure TC11; (c, d) TC11−1.0Nd

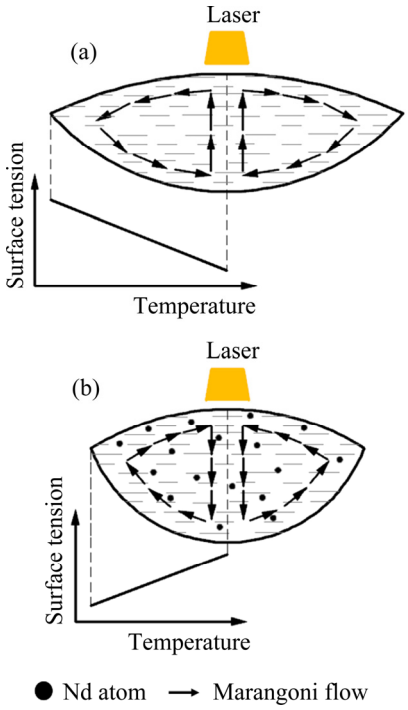

Fig. 11 Schematic diagrams of Marangoni convection: (a) Pure metal; (b) Metal containing surface-active element

convection in the melting pool changes accordingly (as shown in Fig. 11(b)). For titanium alloys, rare-earth elements are surface-active elements. Therefore, the added Nd affects the Marangoni convection and makes the melting pool deeper. Based on the above, under the same laser parameter, the rare-earth added titanium alloys should use a larger height for each layer in future LAM processing.

As can be seen in Figs. 3 and 4, the columnar-to-equiaxed transition (CET) takes place in single-layer specimens. CET is caused by the formation of equiaxed grains at the front of epitaxial growth of columnar grains, which inhibits the growth of columnar grains [4,28]. The nucleation of equiaxed grains in front of columnar grains requires two conditions, including sufficient undercooling and heterogeneous nucleation particles [29,30]. The growth restriction factor, Q, is defined as the rate of development of the constitutional undercooling zone during solidification [31] and can be calculated by

$$Q=m_1C_0(k-1) \quad (1)$$

where m_1 is the slope of liquidus, C_0 is the solute concentration in a binary alloy, and k is the partition coefficient [32]. Some researchers have found that Q is effective in predicting the effect of solute on nucleation in titanium alloys [15,33]. The calculated $m_1(k-l)$ values for Nd and some other solutes in TC11 alloy are presented in Table 3. From the data in Table 3, the added Nd in TC11 can improve constitutional undercooling. Unlike the coaxial powder feeding method for additive manufacturing, there is not large number of foreign nucleation sites during the single-layer experiment, which means that some nucleation sites are formed in a melting pool before β-Ti solidifies. The melting point of Nd_2O_3 is 2272 °C, higher than the solidification temperature of TC11 alloy. So, the Nd_2O_3 particles have the potential to be the nucleation sites from the perspective of solidification behavior. In addition, in contrast to pure TC11, no other particles are formed in a large amount in TC11−1.0Nd except for Nd_2O_3 particles (Fig. 8). Therefore, it is reasonable to believe that Nd_2O_3 particles act as the heterogeneous nucleation sites of β-Ti. The specimens containing more Nd have more equiaxed grains due to greater constitutional undercooling and more heterogeneous particles. The irregular change of depth fraction of equiaxed grains zone from 0.1 wt.% Nd to 0.2 wt.% Nd may be related to the consumption of O atoms in the process of forming Nd_2O_3.

Table 3 Calculated $m_1(k-1)$ values for elements in titanium [32]

Solute element	m_1	k	$m_1(k-1)$
Al	−2.1	→1	→0
Zr	−2.4	0.86	0.3
O	27.6	1.37	10.8
Si	−32.5	0.35	21.7
Nd	−3.9	0.19	3.2

The binary phase diagram for the Nd−Ti system is used to explain how Nd_2O_3 particles are formed in Nd added LAM TC11 alloys [10,34]. In general, there is no Ti−Nd binary intermetallic compound under equilibrium condition, and the solid solubility of Nd in titanium is pretty tiny at ambient temperature [34]. In addition, the V and Al elements in titanium significantly reduce the solubility of rare-earth elements in titanium [35]. So, the majority of Nd in TC11 will combine with O to form Nd_2O_3 particles during LAM processing. At the beginning of solidification, some Nd atoms enriched to the frontier of solid/liquid interface

enlarge the constitutional undercooling in TC11 alloy. As the melting point of Nd_2O_3 is 2272 °C, some Nd_2O_3 particles are formed in the liquid phase (L) firstly. After that, β-Ti begins to form in the liquid phase (L). Some Nd_2O_3 particles are trapped in β grains due to the high speed of the solid/liquid interface moving towards the liquid phase [36], while others situate at the grain boundary of β-Ti. The solid solubility of Nd in β-Ti decreases with the temperature, and these insoluble Nd atoms enter the Nd-rich liquid phase ($L1$) (as shown in Fig. 12). This Nd-rich liquid phase ($L1$) in Nd−Ti system alloys can cause liquid phase separation and the attendant monotectic reaction [12,37]. In the Nd-rich liquid phase ($L1$), Nd and O atoms diffuse easier than that in β-Ti, so Nd atoms can continue to combine with O atoms to form Nd_2O_3 particles. Due to the rapid solidification rate of LAM, some Nd atoms still solute in β-Ti. When the alloy cools to the β transformation temperature, the solubility of Nd in alloy has a relatively significant change. Then, the solubility of Nd in the solid phase drops rapidly so that Nd atoms undergo internal oxidation to form Nd_2O_3. As for multilayer specimens, every layer of multilayer specimens experiences thermal cycling processing causing the Nd_2O_3 particles to grow up.

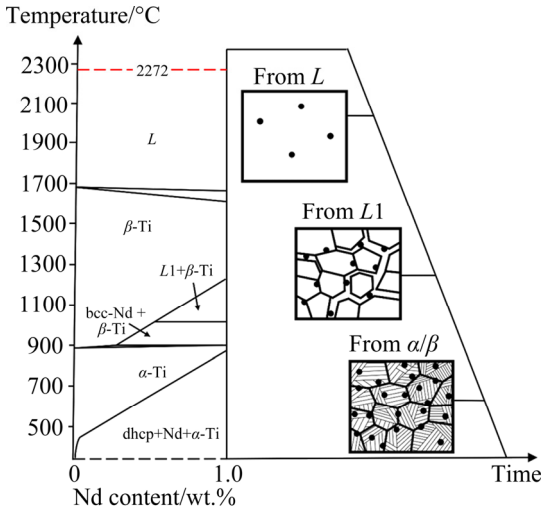

Fig. 12 Phase diagram for Ti−Nd system [10,34]

The refinement mechanisms of Nd in TC11 alloy on β grains and α plates are different. For β grains, firstly, some Nd_2O_3 particles act as the heterogeneous nucleation sites of β-Ti. More nucleation sites lead to more grains, resulting in grain refinement. Secondly, as a surface-active element, Nd can not only change the convection in the melting pool but also reduce the interface energy between the crystal nucleus and the melt [38]. The theoretical nucleation condition of crystal nuclei is [39]

$$\Delta G=\Delta G_i+\Delta G_v=\sigma A+\Delta g\cdot v \quad (2)$$

where ΔG is the nucleation Gibbs free energy change, ΔG_i is the Gibbs interface free energy change, ΔG_v is the Gibbs volume free energy change, σ is liquid/solid interface energy per unit area, A is the surface area of crystal nuclei, Δg is the Gibbs volume free energy change per unit volume and v is the volume of crystal nuclei. The Nd can reduce the nucleation energy by decreasing the interface energy, promoting nucleation to refine grain. In addition, many kinds of rare-earth enriched phases can pin β-Ti grain boundaries, such as Y_2O_3 and La_2O_3 [30,38,40]. Similarly, since Nd_2O_3 particles are situated at the β-Ti grain boundary, they can also play a role in hindering the migration of the grain boundary. For α plates, the main reason for refinement is that some O atoms dissolved in the matrix combine with Nd atoms to form Nd_2O_3. This is also why the intensity of the α-Ti peak and β-Ti peak in the XRD pattern of TC11−1.0Nd shift slightly to the right (Fig. 8). Since the O element is an essential α stable element in titanium alloys, reducing dissolved O atoms in the matrix will increase the β transformation temperature, thereby restraining the growth of α plates in thermal cycling processing [40].

The effect of Nd on the mechanical properties of titanium alloys has multiple mechanisms. First of all, fine Nd_2O_3 particles can inhibit dislocation movement and result in strengthening effect [9,41]. Besides, the refined β grains and α plates have more grain boundary areas, which can also restrict dislocation movement, improving strength and ductility at the same time. However, adding Nd in titanium alloys scavenge some dissolved O atoms in the matrix, which tends to decrease the strength and hardness of the matrix [9]. In the TC11−1.0Nd multilayer specimen, the effect of Nd_2O_3 particles and refined matrix microstructure on tensile strength is great than the effect of dissolved O atoms, so the ultimate tensile strength of the specimen increases. As for the yield strength of the TC11−1.0Nd specimen, since the matrix is more

prone to plastic deformation than the Nd_2O_3 particles, the yield strength mainly depends on the properties of the matrix. Therefore, the yield strength of TC11−1.0Nd decreases, as well as the microhardness of the TC11−1.0Nd matrix. The decrease in relative elongation and fracture surface shrinkage means that the ductility of the TC11−1.0Nd specimen is decreased. The Nd_2O_3 particles may be the main reason for the reduction of ductility. As shown in Fig. 9(d), some broken Nd_2O_3 particles exist in the center of dimples. During tensile testing, the Nd_2O_3 particles can inhibit dislocation movement to increase the strength of the TC11−1.0Nd specimen. When the applied stress reaches a critical value, the Nd_2O_3 particles are broken, and dimples start to form around these broken particles. After that, the cracks unsteadily and rapidly expand along with these broken Nd_2O_3 particles, causing rapid fracture of the TC11−1.0Nd specimen and ultimately resulting in a decrease in the ductility of the specimen.

5 Conclusions

(1) Surface-active element Nd can make the melting pools deeper. Enough Nd can improve CET in titanium alloys. Most Nd atoms combine with O atoms to form Nd_2O_3 particles which are evenly distributed in LAM TC11 alloys without obvious segregation due to the extraordinary nonequilibrium and rapid solidification condition of LAM.

(2) It is found the added Nd has a great refining effect to the β grains and α plates of LAM TC11 alloys. For β grains, the refinement can be attributed to three aspects: the effect of heterogeneous nucleation of Nd_2O_3 particles, the surface activity of Nd, and the pinning effect on the grain boundary of Nd_2O_3 particles. For α plates, the main reason for refinement is that some O atoms dissolved in the matrix combine with Nd atoms to form Nd_2O_3.

(3) The added Nd has multiple influence on the mechanical properties of TC11 alloy. Compared with pure TC11, the ultimate tensile strength of TC11−1.0Nd increases while the yield strength, ductility and hardness decrease.

Acknowledgments

This work was financially supported by the National Natural Science Foundation of China (Nos. 51801009, 52071005), the Youth Talent Support Program of Beihang University, China (No. YWF-21-BJ-J-1143), and Shuangyiliu Fund of Beihang University, China (No. 030810).

References

[1] ELSHAER R N, IBRAHIM K M. Effect of cold deformation and heat treatment on microstructure and mechanical properties of TC21 Ti alloy [J]. Transactions of Nonferrous Metals Society of China, 2020, 30(5): 1290−1299.

[2] HAN L Y, WANG C S. Microstructure and properties of Ti64.51Fe26.40Zr5.86Sn2.93Y0.30 biomedical alloy fabricated by laser additive manufacturing [J]. Transactions of Nonferrous Metals Society of China, 2020, 30(12): 3274−3286.

[3] LI H H, LIU X, LI Y, ZHANG S H, CHEN Y, WANG S W, LIU J S, WU J H. Effects of rare earth Ce addition on microstructure and mechanical properties of impure copper containing Pb [J]. Transactions of Nonferrous Metals Society of China, 2020, 30(6): 1574−1581.

[4] BERMINGHAM M J, MCDONALD S D, DARGUSCH M S. Effect of trace lanthanum hexaboride and boron additions on microstructure, tensile properties and anisotropy of Ti−6Al−4V produced by additive manufacturing [J]. Materials Science and Engineering A, 2018, 719: 1−11.

[5] ZHANG D Y, QIU D, GIBSON M A, ZHENG Y F, FRASERC H L, PRASADE A, STJOHNE D H, EASTONA M A. Refining prior-β grains of Ti−6Al−4V alloy through yttrium addition [J]. Journal of Alloys and Compounds, 2020, 841: 155733.

[6] HOTTA S, YAMADA K, MURAKAMI T, NARUSHIMA T, IGUCHI Y, OUCHI C. β grain refinement due to small amounts of yttrium addition in α+β type titanium alloy, SP-700 [J]. ISIJ International, 2006, 46(1): 129−137.

[7] ZHANG D, GENG K, QIN Y X, LU W J, JI B. The orientation relationship between TiB and RE_2O_3 in in situ synthesized titanium matrix composites [J]. Journal of Alloys and Compounds, 2005, 392: 282−284.

[8] LU W J, XIAO L, XU D, QIN J N, ZHANG D. Microstructural characterization of Y_2O_3 in in situ synthesized titanium matrix composites [J]. Journal of Alloys and Compounds, 2007, 433: 140−146.

[9] SASTRY S M L, PENG T C, BECKERMAN L P. Structure and properties of rapidly solidified dispersion strengthened titanium alloys: Part II. Tensile and creep properties [J]. Metall Mater Trans A, 1984, 15(7): 1465−1474.

[10] SASTRY S M L, MESCHTER P J, O'NEAL J E. Structure and properties of rapidly solidified dispersion-strengthened titanium alloys: Part I. Characterization of dispersoid distribution, structure, and chemistry [J]. Metall Mater Trans A, 1984, 15(7): 1451−1463.

[11] SCHWARTZ D S, FRAUNDORF P, SASTRY S M L. TEM study of B- and Er-containing dispersoids in rapidly solidified dispersion-strengthened titanium and titanium aluminide alloys [J]. Ultramicroscopy, 1991, 37(1−4): 310−317.

[12] COURT S A, SEARS J W, LORETTO M H, FRASER H L. The effect of liquid phase separation on the microstructure of rapidly solidified titanium−rare earth alloys [J]. Materials Science and Engineering A, 1988, 98: 243−249.

[13] ZHU Y Y, CHEN B, TANG H B, CHENG X, WANG H M, LI J. Influence of heat treatments on microstructure and mechanical properties of laser additive manufacturing Ti−5Al−2Sn−2Zr−4Mo−4Cr titanium alloy [J]. Transactions of Nonferrous Metals Society of China, 2018, 28(1): 36−46.

[14] LIU Y T, ZHANG Y Z. Microstructure and mechanical properties of TA15−Ti_2AlNb bimetallic structures by laser additive manufacturing [J]. Materials Science and Engineering A, 2020, 795: 140019.

[15] SAFARZADE A, SHARIFITABAR M, AFARANI M S. Effects of heat treatment on microstructure and mechanical properties of Inconel 625 alloy fabricated by wire arc additive manufacturing process [J]. Transactions of Nonferrous Metals Society of China, 2020, 30(11): 3016−3030.

[16] GOU J, WANG Z J, HU S S, SHEN J Q, TIAN Y B, ZHAO G C, CHEN Y Q. Effects of trace Nb addition on microstructure and properties of Ti−6Al−4V thin-wall structure prepared via cold metal transfer additive manufacturing [J]. Journal of Alloys and Compounds, 2020, 829: 154481.

[17] JIAO Z G, MA C, FU J, CHENG X, TANG H B, LIU D, ZHANG J K. The effects of Zr contents on microstructure and properties of laser additive manufactured Ti−6.5Al−3.5Mo−0.3Si−xZr alloys [J]. Journal of Alloys and Compounds, 2018, 745: 592−598

[18] MEREDDY S, BERMINGHAM M J, STJOHN D H, DARGUSCH M S. Grain refinement of wire arc additively manufactured titanium by the addition of silicon [J]. Journal of Alloys and Compounds, 2017, 695: 2097−2103.

[19] ZHANG H, GU D D, YANG J K, DAI D H, ZHAO T, HONG C, GASSER A, POPRAWE R. Selective laser melting of rare earth element Sc modified aluminum alloy: Thermodynamics of precipitation behavior and its influence on mechanical properties [J]. Additive Manufacturing, 2018, 23: 1−12.

[20] ZHU Y Y, TIAN X J, LI J, WANG H M. The anisotropy of laser melting deposition additive manufacturing Ti−6.5Al−3.5Mo−1.5Zr−0.3Si titanium alloy [J]. Materials & Design, 2015, 67: 538−542.

[21] ZHU Y Y, TIAN X J, LI J, WANG H M. Microstructure evolution and layer bands of laser melting deposition Ti−6.5Al−3.5Mo−1.5Zr−0.3Si titanium alloy [J]. Journal of Alloys and Compounds, 2014, 616: 468−474.

[22] ZHU Y Y, LIU D, TIAN X J, TANG H B, WANG H M. Characterization of microstructure and mechanical properties of laser melting deposited Ti−6.5Al−3.5Mo−1.5Zr−0.3Si titanium alloy [J]. Materials & Design, 2014, 56: 445−453.

[23] ZHU Z S, CAO C X, YAN M G. Low cycle fatigue behavior of a near-α Ti alloy containing rare earth Nd [J]. Materials Science Forum, 2005, 475−479: 599−602.

[24] LI G P, LI D, LIU Y Y, HU Z Q. A study of the microstructure of melt-quenched high-temperature Ti−5Al−4Sn−2Zr−1Mo−0.25Si−1Nd alloy [J]. Materials Letters, 1995, 22(5−6): 237−240.

[25] HEIPLE C R, ROPER J R, STAGNER R T, ADEN R J. Surface active element effects on the shape of GTA, laser and electron beam welds [J]. Welding Journal, 1983, 62(3): 72.

[26] MILLS K C, KEENE B J, BROOKS R F, SHIRALI A. Marangoni effects in welding [J]. Philosophical Transactions of the Royal Society of London. Series A: Mathematical, Physical and Engineering Sciences, 1998, 356(1739): 911−925.

[27] ZHAO C X, KWAKERNAAK C, PAN Y, RICHARDSON I M, SALDI Z, KENJERES S, KLEIJN C R. The effect of oxygen on transitional Marangoni flow in laser spot welding [J]. Acta Materialia, 2010, 58: 6345−6357.

[28] WANG T, ZHU Y Y, ZHANG S Q, TANG H B, WANG H M. Grain morphology evolution behavior of titanium alloy components during laser melting deposition additive manufacturing [J]. Journal of Alloys and Compounds, 2015, 632: 505−513.

[29] ZHU Y Y, TANG H B, LI Z, CHENG X, HE B. Solidification behavior and grain morphology of laser additive manufacturing titanium alloys [J]. Journal of Alloys and Compounds, 2019, 777: 712−716.

[30] BERMINGHAM M J, STJOHN D H, KRYNEN J, TEDMAN-JONES S, DARGUSCH M S. Promoting the columnar to equiaxed transition and grain refinement of titanium alloys during additive manufacturing [J]. Acta Materialia, 2019, 168: 261−274.

[31] MAXWELL I, HELLAWELL A. A simple model for grain refinement during solidification [J]. Acta Metallurgica, 1974, 23(2): 229−237.

[32] BERMINGHAM M J, MCDONALD S D, STJOHN D H, DARGUSCH M S. Beryllium as a grain refiner in titanium alloys [J]. Journal of Alloys and Compounds, 2009, 481: L20−L23.

[33] EASTON M A, STJOHN D H. A model of grain refinement incorporating alloy constitution and potency of heterogeneous nucleant particles [J]. Acta Materialia, 2001, 49: 1867−1878.

[34] MATTERN N, YOKOYAMA Y, MIZUNO A, HAN J H, FABRICHANYA O, HARADA T, KOHARA S, ECKERT J. Experimental and thermodynamic assessment of the Nd−Ti system [J]. Calphad, 2014, 47: 136−143.

[35] SAVITSKII E M, BURKHANOV G S. Phase diagrams of titanium alloys with rare-earth metals [J]. Journal of the Less Common Metals, 1962, 4(4): 301−314.

[36] UHLMANN D R, CHALMERS B, JACKSON K A. Interaction between particles and a solid−liquid interface [J]. Journal of Applied Physics, 1964, 35(10): 2986−2993.

[37] COURT S A, STANLEY J T, KONITZER D G, LORETTO M H, FRASER H L. The microstructure of rapidly solidified and heat-treated Ti alloys containing La [J]. Acta Metallurgica, 1988, 36(6): 1585−1594.

[38] TIAN Y S, CHEN C Z, CHEN L X, HUO Q H. Effect of RE oxides on the microstructure of the coatings fabricated on titanium alloys by laser alloying technique [J]. Scripta Materialia, 2006, 54: 847−852.

[39] KURZ W, FISHER D J. Fundamentals of solidification [M]. Trans Tech Publication Switzerland, 1998: 71−92.

[40] CUI W F, LIU C M, ZHOU L, LUO G Z. Characteristics of

microstructures and second-phase particles in Y-bearing Ti-1100 alloy [J]. Materials Science and Engineering A, 2002, 323(1/2): 192−197.

[41] SANKARAN K K, SASTRY S M L, PAO P S. The effects of second-phase dispersoids on the deformation behavior of titanium [J]. Metall Mater Trans A, 1980, 11(1): 196−198.

Nd 添加对激光增材制造 TC11 钛合金显微组织与拉伸性能的影响

严文高[1]，王华明[1]，汤海波[1,2]，程 序[1,2]，朱言言[1,2]

1. 北京航空航天大学 前沿科学技术创新研究院 大型金属构件增材制造国家工程实验室，北京 100191；
2. 北京航空航天大学 宁波创新研究院，宁波 315800

摘 要：制备不同 Nd 含量的 TC11 钛合金单道熔覆和单道多层激光增材制造(LAM)试样，研究 Nd 添加对显微组织和力学性能的影响。结果表明，随着 Nd 含量增加，单道熔覆熔池的深宽比增加，并且在熔池中发生柱状晶向等轴晶的转变(CET)。单道多层 TC11−1.0Nd 试样的原始 β 晶粒尺寸和 α 片层宽度相比纯 TC11 样品的明显减小，主要原因是熔池快速凝固时优先形成平均尺寸约 1.51 μm 的均匀弥散分布的细小 Nd_2O_3 析出相，在后续凝固和固态相变中作为异质形核质点而细化组织。由于 Nd 对显微组织的多重影响，激光增材制造 TC11−1.0Nd 相比纯 TC11 样品抗拉强度提高，而屈服强度、伸长率和显微硬度降低。

关键词：激光增材制造；钛合金；稀土元素；显微组织；晶粒细化；力学性能

(Edited by Bing YANG)